Title: Novel DNA endonuclease activity of human ERK1 protein

Authors: Sangmin Ju[1]†, Jaehyeon Jeong[2]†, Bin Chan Joo[3]†, Soo Jin Lee[1,4], Sanzhar Tarassov[2]‡, Jeong Ho Chang[4], Jae-Han Jeon[5], Stuart K. Calderwood[6], Yeon Ui Lee[3], Heeyoun Bunch[1,2]*

Affiliations:

[1]School of Applied Biosciences, College of Agriculture & Life Sciences, Kyungpook National University; Daegu, 41566, Republic of Korea.

[2]Department of Applied Biosciences, Kyungpook National University; Daegu, 41566, Republic of Korea.

[3]Department of Physics, Chungbuk National University; Cheongju, 28644, Republic of Korea.

[4]Department of Biomedical Convergence Science & Technology, Kyungpook National University; Daegu, 41566, Republic of Korea.

[5]School of Medicine, Kyungpook National University; Daegu, 41944, Republic of Korea.

[6]Department of Radiation Oncology, Beth Israel Deaconess Medical Center, Harvard Medical School; Boston, 02115, USA.

*Corresponding author. Email: heeyounbunch@gmail.com (H.B.)

†These authors contributed equally to this work

‡Present addresses. ‡S. Tarassov, Department of Chemistry & Bioengineering, Vilnius Tech University; Vilnius, 10223, Lithuania.

Abstract: ERK1 is a key kinase in the mitogen-activated protein kinase pathway, which transduces extracellular signals into cellular responses. Following triggering of the pathway, cytosolic ERK1 is phosphorylated and translocated into the nucleus to activate DNA-bound factors and target genes. This study reports a novel role of human ERK1 as a DNA endonuclease to catalyze single-strand DNA breaks without sequence-specificity. ERK1 catalysis required magnesium ion and was independent of ATP. Biochemical and structural analyses indicated that the ERK1 N-terminal domain allosterically modulates substrate binding and catalytic rate. Fluorescence imaging showed that ERK1 interacts with cytoplasmic DNAs in condensates. Collectively, our study reveals an unprecedented role of ERK1 in breaking DNA molecules, a finding which highlights the potential of ERK1 to regulate cytoplasmic DNA topology and fate.

Main Text: The mitogen-activated protein kinase (MAPK) pathway consists of protein phosphorylation cascades that link extracellular signals to cellular responses, including gene regulation in plants and mammals (*1*). The MAPK pathway is crucial for controlling cell proliferation, DNA repair, apoptosis, and inflammation (*2*). Deregulation of the MAPK pathway is closely associated with cancer and neurodegenerative diseases; many compounds inhibiting protein kinases in the MAPK pathway have been developed and clinically tested for treatment of these pathologies (*3, 4*). Additionally, viral infections take advantage of MAPK pathway activation to promote the replication of the viral genome (*5*), indicating an important role of MAPK in viral and immune responses. MAPK1 and MAPK3 (ERK2 and ERK1, respectively) are phosphorylated and activated by MAPKK (MEK1/2) in the cytoplasm and are translocated into the nucleus, where they phosphorylate and activate nuclear transcription factors such as ELK1 and MYC (*3, 6-8*).

Our previous study revealed that ERK1 and ERK2 have different roles in the transcription of *EGR1* and *FOS*, representative immediate early genes (IEGs) and the first responder genes for cell cycle progression (*9*). ERK2 activates IEG transcription, whereas ERK1 represses it. Mechanistically, ERK2 modulates topoisomerase IIβ (TOP2B) catalytic activity to relax positive DNA supercoiling and delay negative DNA supercoiling (*9*). Meanwhile, this study led us to speculate that ERK1 may possess a non-canonical enzymatic activity to resolve DNA supercoiling by itself, a hypothesis urgently and importantly needing validations. Thus, our present study has investigated the potential role of ERK1 as a DNA topology factor and nuclease, and further explored the physiological significance and implication of the new ERK1 function.

Human ERK1 possesses DNA endonuclease activity.

We compared first constitutively kinase-active human ERK mutants (*10*) —ERK1m ($R^{84}S$) and ERK2m ($R^{67}S$) — to investigate the basis for the differential properties of these enzymes in terms of endonuclease activities (*9*). These proteins were therefore expressed in *Escherichia coli* and purified using Ni affinity and gel filtration columns side-by-side (**fig. S1A**). Interestingly, ERK1m, but not the control (CTRL, ERK storage buffer only) or ERK2m, converted the negatively supercoiled substrate pBR322 (4361 bp) to nicked (or open-circular, OC) and linearized pBR322 plasmid in DNA relaxation assays (**Fig. 1A**). It should be noted that proteins were extracted by phenol, chloroform, and isoamyl alcohol immediately after the reaction, and so only DNA was separated and visualized on the gels in the DNA relaxation assay. To determine whether WT ERK1 also possessed a similar topological/DNase activity to that of ERK1m, ERK1 (K1) and ERK1m (K1m) were purified and compared side-by-side and confirmed by immunoblotting (**Fig. 1B**). TOP2B was included as a control to compare with ERK1s for their band patterns, as TOP2B is known to generate partially relaxed plasmid species by removing DNA writhes one at a time (**fig. S1B**). The relaxation assay results showed that the enzymatic activities of ERK1 and ERK1m were comparable, yet distinctive from those of TOP2B (**Fig. 1, C** and **D**). ERK1 and ERK1m did not relax DNA supercoiling partially, as shown in the TOP2B reaction, but generated primarily nicked plasmids, then accumulated linearized ones (**Fig. 1C**). ERK1 did not require ATP to convert the supercoiled, circular plasmids to nicked or linear ones (**Fig. 1E**). In addition, the presence of magnesium ion (Mg^{2+}) in reaction was critical for this

endonuclease function of ERK1 and was not substitutable with other divalent ions, such as zinc or calcium (**Fig. 1F**).

ERK1 catalyzes random single-strand DNA breaks on circular DNA.

To further characterize the unexpected DNA relaxing function of ERK1, the enzyme concentration was titrated at 0, 2.5, 25, 50, 125, and 250 nM, and the reaction was allowed to proceed for 3 h at 30 °C in DNA relaxation assays. Nicked and linearized plasmids, the catalysis products, were accumulated in a dose-dependent manner (**Fig. 2, A** and **B** and **fig. S2A**). Nicked plasmid DNA appeared to be formed first, and then a portion of the products was converted to linearized ones (see 50, 125, and 250 nM in **Fig. 2A**). Time-course experiments with 230 nM ERK1 and 3.5 nM pBR322 plasmids showed almost complete supercoiled plasmid removal at 1 h timepoint and slowly increased levels of linearized bands at 3 and 5 h time points (**Fig. 2, C** and **D** and **fig. S2B**). Under the assumption that the substrates were circular, supercoiled DNA and that the products were the lost substrates converted to either nicked or linearized ones, K_{cat} of ERK1 was calculated to be approximately 0.0005 min^{-1}.

Next, we mapped the DNA sequences recognized for digestion by ERK1. Two enzymes, which cut pBR322 at only one restriction site, HindIII (Hind) and NruI (Nru), were used (**Fig. 2, E** and **F**). We rationalized that a specific ERK1-catalyzed site(s) could be mapped if ERK1 linearized the circular plasmids in a sequence-restricted manner, by cutting it at a specific site(s). As shown in **Fig. 2G**, after pBR322 was incubated with ERK1 (lane 3; K1), the linearized plasmids were gel-purified (lane 4; GE) and digested by Hind or Nru. Interestingly, either enzyme digestion produced multiple bands, accompanied by intensified smears rather than specific few bands, (lanes 5,6; Nru, Hind). These data suggested that ERK1 digests the plasmid at random sites in circular DNA in a sequence-unspecific manner. We propose that, random DNA breaking near the restriction enzyme sites and the replication origin, relatively underwound in the negative supercoiled plasmid, could produce thicker bands of slightly lower molecular weights than linearized vector and other bands observed in our data (e.g. 2536 and 1824 bp for Nru; **Fig. 2H**).

N-terminal domain of ERK1 determines nucleolytic efficiency.

Human ERK1 and ERK2 are 82.6% identical in amino acid sequences with distinctive N-terminal domains (*11*). We therefore examined ERK1 and ERK2 N-terminal sequences for likely critical residues and mutated two consecutive arginines, at 15 and 16 to single or double alanine mutations within the region uniquely present in ERK1 (11–27 a.a.; **Fig. 3A**). The three mutant ERK1 proteins, $R^{15}A$ (15A), $R^{16}A$ (16A), or $R^{15}A/R^{16}A$ (Double) mutants were bacterially expressed and purified (**Fig. 3B**). WT and mutant ERK1 proteins at concentrations 0, 60, 120, and 200 nM were incubated with negatively supercoiled pBR322 for 15 min before resolving the DNA molecules on the gel. 15A showed slightly inferior activity, whereas 16A ERK1 showed a notably enhanced nuclease activity, compared with the WT. The double mutant showed a similar activity to the one of the WT (**Fig. 3, C** and **D** and **fig. S3A**). Additionally, three residues, negatively charged glutamate, E^{13}, E^{18}, and E^{27} were individually mutated to alanine (**Fig. 3E**). The mutants were purified (**Fig. 3F**) and compared with the WT in the same experimental conditions as described in **Fig. 3C**. $E^{13}A$ (13A) and $E^{27}A$ (27A) exhibited enhanced nuclease activities, whereas $E^{18}A$ (18A) showed similar digestion efficiencies, compared to the WT (**Fig.**

3, G and **H** and **fig. S3B**). These data suggested that the N-terminal region spanning residues 11–27 suppresses the nuclease activity of ERK1 involving electrostatic interactions through E^{13}, R^{16}, and E^{27}.

Binding affinity to substrate, pBR322, was next monitored for WT, 13A, and 16A ERK1 proteins using the gel electrophoretic mobility shift assay (EMSA). Agarose gel, instead of polyacrylamide one, was used for the assay owing to a large molecular weight (4361 bp) and bulky shapes of the plasmid DNA (*12*). The WT or mutant ERK1s were titrated at concentrations 0, 1, 2.5, and 5 μM with 1 nM pBR322 for 10 min at room temperature before loading onto the gel. Despite the large size and bulky shape of DNA, higher gel percentages were needed to visualize band-shift because of the molecular weight of ERK1 (44 KDa), which is equivalent to approximately 70 bp double stranded DNA (dsDNA). These challenges limited the resolution only to linearized DNAs with sizes below 5 Kbp. In the absence of Mg^{2+}, a dose-dependent band shift was observed, with major bands for the SC DNA-protein complexes and minor bands for the OC DNA-protein complexes (**Fig. 3I**). The two mutants, 13A and 16A, and especially 13A, appeared to have a reduced binding affinity to the SC DNA, compared to the WT (**Fig. 3I**). In the presence of Mg^{2+}, SC, linear, and OC DNA bands were shown, as expected, because ERK1 could actively catalyze SC DNAs into OC and OC to linear DNAs (**Fig. 3J**). Despite showing a lower substrate binding affinity without Mg^{2+}, 13A ERK1 produced linear DNA more efficiently than WT or 16A in the presence of Mg^{2+} (**Fig. 3J**). All three proteins bound to linearized plasmid DNA as well as SC and OC DNA to shift their mobility, yet with different affinities (**Fig. 3J**).

Artificial intelligence-predicted ERK1 structure model.

We investigated the ERK1 protein sequence and found that it lacks known DNA endonuclease or nickase motifs. In addition, currently available human ERK1 and ERK2 structures have limited information because they were co-crystalized with other peptides and/or inhibitors and omitted the apparently flexible N- and C-terminal domains (*13, 14*). Therefore, we employed an artificial intelligence (AI)-based tool, AlphaFold 3 to predict ERK protein structures and to evaluate the structural potentials to interact with and catalyze DNA molecules (*15*). AI-predicted full-length ERK1 (379 a.a., 44 KDa) and ERK2 (360 a.a., 42 KDa) structures showed overall similarities and yet distinctive N-terminal domains and surface contours (**Fig. 4A** and **fig. S4A**). Next, ERK1 was co-structured with DNA segments of pBR322. It was found that ERK1-DNA interaction was established only in the inclusion of Mg^{2+} in the algorithm (**fig. S4B**). Interestingly, the structure of the ERK1-DNA (pBR322 DNA segments including 2292–2319)-Mg^{2+} complex indicated a DNA binding cleft and a Mg^{2+} binding site in ERK1, where N^{171} and D^{184} could have electrostatic interactions with Mg^{2+} within 2.7 Å proximities (**Fig. 4B** and **fig. S4C** and **Movie S1**). Mutating N^{171} and D^{184} to alanine dissociated Mg^{2+} from the binding pocket (**fig. S4D**). The distance between Mg^{2+} and the DNA backbone was about 6.8 Å (**Fig. 4B**). We speculated the possibility of hydrated Mg^{2+} or titratable residues near the DNA binding site, such as K^{168} and S^{170}, which were located within 5 Å from the Mg^{2+} ion, for mediation of DNA strand break (**fig. S4E**).

A comparison between the crystal (complexed with a docking peptide and missing N- and C-terminal domains, PDB ID: 4H3Q) and AI-predicted (full-length) structures of ERK2 showed

overall similarities, supporting confidence in AI structures (**Fig. 4C** and **fig. S4F**). Similar to those of ERK1, AI-predicted ERK2 structures showed DNA (2292–2319 of pBR322) and Mg^{2+} binding sites (**Fig. 4D**). However, the distances between Mg^{2+} and N^{154} and D^{167} and between Mg^{2+} and DNA backbone were overall farther, 3.1 Å and 8.1 Å, respectively, compared to those of ERK1, suggesting weaker interactions (**Fig. 4D**). In addition, we compared AI-predicted WT, 13A, and 16A ERK1 structures (**Fig. 4E**). Interestingly, these mutants rotated the flexible N-terminal domain in different angles, allosterically modulating the conformation of the hinge and DNA binding domains to shorten the distances between the critical Mg^{2+} ion and the two coordinating amino acids (**Fig. 4, E** and **F** and **fig. S4G**). Mechanically, the structures suggested that the strength of Mg^{2+} binding to the ERK1 enzyme might be important for catalytic efficiency.

ERK1 interacts with and destabilizes cytoplasmic DNA.

Our previous study showed that ERK1 (and also ERK2) in HeLa nuclear extracts rarely bound to the DNA, although bacterially purified ERK1 did in the immobilized template assay (**fig. S5A)**(*9*). One possible difference between these two protein groups is post-translational modification, as ERK1 is known to be translocated into the nucleus in a phosphorylation-dependent manner (*16*). In addition, recent studies have identified a variety of cytoplasmic DNA (cytoDNA) species in humans, including extrachromosomal DNA, mitochondrial DNA, micronuclei, cytoplasmic chromatin fragments, and viral and bacterial DNA (*17-22*). Therefore, we hypothesized that ERK1 in the cytoplasm might interact with cytoDNAs. To test this hypothesis, ERK1 and cytoDNA in HEK293T cells were monitored using an ERK1 antibody and DAPI over-exposure (*23-26*), respectively, under a high-resolution fluorescence microscopy. DNA-RNA probes based on chromosome 7p11.2 were tested as controls (**fig. S5B**), which confirmed that DAPI stains DNA, but not RNA. ERK1 was located primarily in the cytoplasm in typical cells, and a portion of the ERK1 molecules appeared to be colocalized with dsDNAs, visualized by over-exposed DAPI ($DAPI^{o}$, F1–3, **Fig. 5A** and **fig. S5C**). Super-resolution imaging of focal spots, F1–3, strikingly, showed that a large number of ERK1 molecules (44 KDa in approximately 2.4 nm) interacted with thousands of dsDNA molecules sizing approximately 20 nm, which is equivalent to approximately 55 Kbp dsDNA, forming nano-scale condensates (**Fig. 5B**).

Next, we hypothesized that ERK1 knock-out (KO) may increase the number of cytoDNAs and their puncta in cells because ERK1 breaks and destabilizes dsDNA with its DNA endonuclease activities *in vitro*. CRISPR-Cas 9-edited ERK1 KO HEK293T cells were used to validate the hypothesis (**Fig. 5C**). It was noted that cytoDNA puncta were more readily visible in ERK1 KO cells under the microscope, which was composed of a number of dsDNA molecules (**Fig. 5D**). Consistently, compared to the WT HEK293T cells, ERK1 KO cells exhibited significantly increased counts of cytoDNA puncta (**Fig. 5, E** and **F** and **fig. S5D**).

Together, these findings support a novel enzymatic function of human ERK1 protein as a DNA endonuclease that nicks and linearizes circular dsDNA. ERK1 generates ssDNA breaks to induce dsDNA breaks stepwise. It is also noted that protein kinases hydrolyze ATP to transfer the γ-phosphate of a purine nucleotide triphosphate covalently to the hydroxyl groups of their

substrates (*27*). The new endonuclease role of ERK1, a transcription factor and kinase, brings up the question of whether more DNA-binding transcription factors with phosphotransferase function might be able to break DNA strand(s) by redox reactions. Our AI-based structural model illustrates ERK1-DNA interaction and the important role of Mg^{2+} for ERK1-mediated DNA catalysis. DNA break is a critical cellular event, linked to DNA topological changes and recombination, gene regulation, genomic mutation/instability, microbial defense, cell fate, and more (*28-33*). Therefore, our finding that ERK1 has a novel endonuclease activity is important and associates a variety of physiological and clinical implications. Finally, cytoDNAs have emerged as important regulators of inflammation, immunity, and degenerative diseases (*34-36*). ERK1 interacting with cytoDNAs shown in this study suggests potentially important roles of cytoplasmic ERK1 to regulate the fate and topology of cytoDNAs, which awaits future studies.

Materials and Methods

Protein preparation

Bacterial expression vectors expressing human WT and ERK1 mutant (R84S, ERK1m) and mouse ERK2 mutant (R67S, ERK2m) were gifted by Drs. N. Soudah and D. Engelberg at the Hebrew University of Jerusalem. As described in our previous study, human ERK2m was generated from mouse ERK2m by Quikchange mutagenesis (*9*). The recombinant ERK1 proteins were expressed in *E. coli* BL21(DE3) in LB media containing 50 μg/L kanamycin (Applichem) and induced at 20 °C for 18 h by 0.3 mM IPTG. In the following purification steps, protein samples and buffers were kept at 4 °C. Cells were harvested by centrifugation, resuspended in a buffer containing 20 mM Tris, pH 8.0, 250 mM NaCl, 0.05% β-mercaptoethanol, 0.2% Triton X-100, and 5% glycerol (Affymetrix), and protease inhibitors. Cells were lysed by ultrasonication (Sonics, VCX-500/750) and centrifuged to collect the supernatant, which was loaded onto a HisTrap FF column (GE Healthcare). After eluting the bound proteins with a linear gradient of imidazole, protein-containing fractions were concentrated and loaded onto a HiPrep 16/60 Sephacryl S-300 HR column (GE Healthcare) and eluted using a buffer (ERK1 storage buffer; used as the control, [CTRL]) containing 20 mM Tris, pH 7.5, 150 mM NaCl, and 2 mM DTT. Human topoisomerase IIβ (TOP2B) was prepared and purified as previously described (*34, 35*). Resulting, purified proteins were confirmed by silver-staining and immunoblotting. Protein concentrations were determined by the Bradford assay (Bio-Rad).

Cloning & ERK1 mutagenesis

pET-15b WT ERK1 plasmid was used as a template to generate six ERK1 mutants: $R^{15}A$, $R^{16}A$, Double ($R^{15}A/R^{16}A$), $E^{13}A$, $E^{18}A$, and $E^{27}A$. Site-directed point mutations were generated by polymerase chain reaction (PCR). Each reaction contained 58 ng of template plasmid DNA, 1 U of KOD FX neo polymerase (TOYOBO), 0.25 μM primers (**Table S1**), KOD FX neo buffer and 0.4 mM dNTPs as final concentrations. Thermal cycles were carried out as follows: 30 s at 95 °C for initial denaturation, followed by 16 cycles of 30 s at 95 °C, 1 min at 55 °C, 4 min at 68 °C, and 5 min at 68 °C for final extension. To remove template DNA, all PCR products were incubated with restriction endonuclease DpnI (New England Biolabs) at 37 °C for 1 hour to overnight. DpnI mixtures were transformed into *E. coli* (DH5α). Plasmids were extracted from 5 mL of saturated bacterial culture using the NucleoSpin plasmid (Macherey-Nagel) or QIAprep Spin Miniprep (Qiagen) kits, following the manufacturers' instruction.

Supercoiled DNA Relaxation assay

Negatively supercoiled pBR322 was purchased from ThermoFisher Scientific and Inspiralis (Cat. SD0041 and S5001, respectively). To obtain the linearized plasmid, 0.25 μg of the plasmid was incubated with a restriction endonuclease HindIII (R0104S, New England BioLabs) at 37 °C for 3 h. The relaxation assay buffer included 50 mM Tris-HCl (pH 7.5), 125 mM NaCl, 10 mM $MgCl_2$, 5 mM DTT, 0.1 mg/mL BSA as final concentrations. Each reaction included 0.25 or 0.5 μg of negatively supercoiled pBR322 as the substrate for ERK or TOP2B. ERK protein at indicated concentrations or an equal volume of the ERK storage buffer was added to initiate the reaction. Dephosphorylated, deubiquitinated TOP2B (112 pM) or an equal volume of the buffer control was used as a control. The catalytic reaction of TOP2B was induced by adding ATP to 1 mM final concentration. ERK- or TOP2B-catalysis of plasmid DNA were allowed at 30 °C for indicated durations (0 to 5 h). The reaction was terminated by adding equal volumes of both cold STOP solution [40% glycerol, 100 mM Tris-HCl (pH 8.0), 10 mM EDTA, 0.5 mg/mL bromophenol blue] and cold phenol-chloroform-isoamyl alcohol (PCI) on ice. The mixture was thoroughly mixed and centrifuged at 8000 rpm for 2 min. The aqueous, upper phase was carefully removed and loaded onto a 0.8–1% agarose gel. The DNA on the gel was visualized by staining in 0.01% ethidium bromide solution for 10 min and sufficient destaining in water. For immunoblotting, 10% of the reaction mixture was reserved before adding PCI and stored at –70 °C until the analysis.

Immunoblotting

WT and ERK1 knock-out (KO) HEK293T cells were grown to approximately 70%–80% confluence in 6-well plates, washed with cold PBS, and then collected with RIPA buffer (Cell Signaling Technology). The protein concentrations of the cell lysates were measured using the Bradford assay (Bio-Rad). From the measured protein concentrations, equal amounts of proteins were loaded onto an SDS-polyacrylamide gel. The separated proteins were transferred to a nitrocellulose membrane (GE Healthcare). Primary antibodies were used for probing β-ACTIN (MA5-15739, Invitrogen), MED23 (A300-425A, Bethyl Laboratories), HSP70 (sc-32239, Santa Cruz Biotechnology), TOP2B (Cat. 50-155-8867, Fisher Scientific), ERK1 (ab32527, Abcam), ERK1/2 (ab17942, Abcam), and ERK2 (ab32081, Abcam). Each antibody was diluted in 5% skim milk (Bio-Rad) solution. After the primary antibody incubation, the membranes were rinsed twice and washed four times, each for 10 min, with PBST solution [137 mM NaCl, 2.7 mM KCl, 4.3 mM Na_2HPO_4, 1.5 mM KH_2PO_4, 0.1% (v/v) Tween-20 and pH 7.4]. HRP-conjugated rabbit (#7074, Cell Signaling Technology) or mouse (#7076, Cell Signaling Technology) secondary antibodies, were diluted in 5% skim milk and incubated with the membranes. After incubation, the membranes were rinsed twice and washed four times with PBST solution, each for 10 min. Western Blotting Luminol Reagent (sc-2048, Santa Cruz Biotechnology) was used to develop signals.

Cell culture

WT and CRISPR/Cas 9 homozygous ERK1 KO (1 bp deletion in exon 1) HEK293T cells were purchased from Abcam (Cat. ab266519). Cells were expanded and maintained in DMEM (Cytiva Hyclone) supplemented with 10% fetal bovine serum (FBS, Gibco) and 1% penicillin/streptomycin (Thermo Fisher), following ATCC guidelines.

Immunofluorescence analysis

WT and ERK1 KO HEK293T cells were seeded onto coverslips and allowed to adhere. Cells were fixed with 4% paraformaldehyde (PFA) for 20 min at 4 °C, followed by permeabilization with 0.05% Triton X-100 in PBS for 5 min at RT. After washing, cells were blocked with 5 mg/mL BSA in PBST (0.04% Tween-20 in PBS) for 30 min at RT to minimize nonspecific binding. Cells were then incubated overnight at 4 °C with a primary anti-ERK1 antibody (sc-271269, Santa Cruz Biotechnology) diluted in a blocking buffer. After extensive washing with PBST, cells were incubated with an Alexa Fluor 647-conjugated secondary antibody for 1h at RT in the dark. Nuclei were counterstained with 4,6-diamidino-2-phenylindole (DAPI) for 5 min. Conventional fluorescence microscopy was performed using a confocal microscope (K1-Fluo, K1 nanoscope; Nanoscope Systems). For DNA-RNA fluorescence in situ hybridization (FISH) analysis, EGFR FISH probe (EGFR-20RE, Empire Genomics) generated from 7p11.2 locus encompassing a 295 Kbp genomic region was used, according to the manufacturer's instruction, omitting the use of RNases. Fluorescence images were acquired using a photomultiplier tube (PMT) with excitation lasers, dichroic mirrors, and emission filters. For DAPI fluorescence imaging, a 405 nm linearly polarized excitation laser was used, with emissions collected through a 500–550 nm bandpass filter. For fluorescence imaging of FISH probes, a 561 nm linearly polarized excitation laser was used, and emissions were collected 590–650 nm bandpass filter. For Alexa 647 fluorescence imaging, a 561 nm linearly polarized excitation laser was used, and emissions were collected through a 700–760 nm bandpass filter. A 100× oil immersion objective (NA = 1.49, Olympus) and a 70-second exposure time were applied. Polarization-modulated super-resolution imaging was performed using a confocal microscope with modifications (*37*). The polarization states of the excitation laser beam were manipulated using a quarter-wave plate (QWP) and a liquid crystal variable retarder (LCVR; LCC1513-A, Thorlabs). Six distinct polarization states were applied during imaging. Fluorescence signals were detected via PMT arrays, with phase retardance of the LCVR programmed using external voltages throughout the acquisition of 3000 frames. Imaging was performed using a 100× oil immersion objective (NA = 1.49, Olympus), with an exposure time of 600 ms per frame. Single-molecule localization reconstruction was performed using the ThunderSTORM plug-in for ImageJ (*38*). The raw dataset contained 3000 frames with 1024 × 1024 pixels (pixel size: 85 nm). Localization was achieved using an 8-neighborhood connectivity algorithm with a Gaussian point spread function (PSF) fitting model. Image filtering involved third-order B-spline wavelets, and sub-pixel localization was applied with a 4-pixel fitting radius and 20× magnification.

Statistical analysis

The Student's t-test ($p < 0.05$, one- or two-sided) was performed to determine statistical significance. Graphs were generated using the Prism 9 software.

References and Notes

1. A. F. Peterson *et al.*, Systematic analysis of the MAPK signaling network reveals MAP3K-driven control of cell fate. *Cell Syst* **13**, 885-894 e884 (2022).
2. W. Zhang, H. T. Liu, MAPK signal pathways in the regulation of cell proliferation in mammalian cells. *Cell Res* **12**, 9-18 (2002).

3. F. Liu, X. Yang, M. Geng, M. Huang, Targeting ERK, an Achilles' Heel of the MAPK pathway, in cancer therapy. *Acta Pharm Sin B* **8**, 552-562 (2018).
4. F. Khojasteh Poor *et al.*, Mini review: The FDA-approved prescription drugs that target the MAPK signaling pathway in women with breast cancer. *Breast Dis* **40**, 51-62 (2021).
5. B. K. Lim *et al.*, Coxsackievirus B3 replication is related to activation of the late extracellular signal-regulated kinase (ERK) signal. *Virus Res* **113**, 153-157 (2005).
6. A. V. Khokhlatchev *et al.*, Phosphorylation of the MAP kinase ERK2 promotes its homodimerization and nuclear translocation. *Cell* **93**, 605-615 (1998).
7. Y. Shindo *et al.*, Conversion of graded phosphorylation into switch-like nuclear translocation via autoregulatory mechanisms in ERK signalling. *Nat Commun* **7**, 10485 (2016).
8. A. J. Whitmarsh, P. Shore, A. D. Sharrocks, R. J. Davis, Integration of MAP kinase signal transduction pathways at the serum response element. *Science* **269**, 403-407 (1995).
9. H. Bunch *et al.*, ERK2-topoisomerase II regulatory axis is important for gene activation in immediate early genes. *Nat Commun* **14**, 8341 (2023).
10. V. Levin-Salomon, K. Kogan, N. G. Ahn, O. Livnah, D. Engelberg, Isolation of intrinsically active (MEK-independent) variants of the ERK family of mitogen-activated protein (MAP) kinases. *J Biol Chem* **283**, 34500-34510 (2008).
11. M. Marchi *et al.*, The N-terminal domain of ERK1 accounts for the functional differences with ERK2. *PLoS One* **3**, e3873 (2008).
12. S. K. Mauldin, R. C. Getts, W. Liu, T. D. Stamato, DNA-PK-dependent binding of DNA ends to plasmids containing nuclear matrix attachment region DNA sequences: evidence for assembly of a repair complex. *Nucleic Acids Res* **30**, 4075-4087 (2002).
13. G. Gogl, I. Toro, A. Remenyi, Protein-peptide complex crystallization: a case study on the ERK2 mitogen-activated protein kinase. *Acta Crystallogr D Biol Crystallogr* **69**, 486-489 (2013).
14. T. Kinoshita *et al.*, Crystal structure of human mono-phosphorylated ERK1 at Tyr204. *Biochem Biophys Res Commun* **377**, 1123-1127 (2008).
15. J. Abramson *et al.*, Accurate structure prediction of biomolecular interactions with AlphaFold 3. *Nature* **630**, 493-500 (2024).
16. D. S. Lidke *et al.*, ERK nuclear translocation is dimerization-independent but controlled by the rate of phosphorylation. *J Biol Chem* **285**, 3092-3102 (2010).
17. K. N. Miller *et al.*, Cytoplasmic DNA: sources, sensing, and role in aging and disease. *Cell* **184**, 5506-5526 (2021).
18. C. Bailey *et al.*, Origins and impact of extrachromosomal DNA. *Nature* **635**, 193-200 (2024).
19. L. T. Geller *et al.*, Potential role of intratumor bacteria in mediating tumor resistance to the chemotherapeutic drug gemcitabine. *Science* **357**, 1156-1160 (2017).
20. D. Nejman *et al.*, The human tumor microbiome is composed of tumor type-specific intracellular bacteria. *Science* **368**, 973-980 (2020).
21. L. T. Pecorino, R. G. W. Verhaak, A. Henssen, P. S. Mischel, Extrachromosomal DNA (ecDNA): an origin of tumor heterogeneity, genomic remodeling, and drug resistance. *Biochem Soc Trans* **50**, 1911-1920 (2022).
22. L. Yu, P. Liu, Cytosolic DNA sensing by cGAS: regulation, function, and human diseases. *Signal Transduct Target Ther* **6**, 170 (2021).
23. M. Dellinger, M. Geze, Detection of mitochondrial DNA in living animal cells with fluorescence microscopy. *J Microsc* **204**, 196-202 (2001).

24. S. Kobayashi *et al.*, BAF is a cytosolic DNA sensor that leads to exogenous DNA avoiding autophagy. *Proc Natl Acad Sci U S A* **112**, 7027-7032 (2015).
25. T. Haraguchi *et al.*, Transfected plasmid DNA is incorporated into the nucleus via nuclear envelope reformation at telophase. *Commun Biol* **5**, 78 (2022).
26. C. Estell, E. Stamatidou, S. El-Messeiry, A. Hamilton, In situ imaging of mitochondrial translation shows weak correlation with nucleoid DNA intensity and no suppression during mitosis. *J Cell Sci* **130**, 4193-4199 (2017).
27. L. Castelo-Soccio *et al.*, Protein kinases: drug targets for immunological disorders. *Nat Rev Immunol* **23**, 787-806 (2023).
28. H. Bunch *et al.*, DNA topological regulation by topoisomerase IIβ-DNA-PK interaction is important for controlled hypoxia-inducible gene expression. *bioRxiv*, 2025.2001.2006.631366 (2025).
29. I. Dereli *et al.*, Seeding the meiotic DNA break machinery and initiating recombination on chromosome axes. *Nat Commun* **15**, 2941 (2024).
30. A. Tubbs, A. Nussenzweig, Endogenous DNA Damage as a Source of Genomic Instability in Cancer. *Cell* **168**, 644-656 (2017).
31. P. Widlak, L. Y. Li, X. Wang, W. T. Garrard, Action of recombinant human apoptotic endonuclease G on naked DNA and chromatin substrates: cooperation with exonuclease and DNase I. *J Biol Chem* **276**, 48404-48409 (2001).
32. Y. Yu *et al.*, Yeast EndoG prevents genome instability by degrading extranuclear DNA species. *Nat Commun* **15**, 7653 (2024).
33. H. Bunch *et al.*, Transcriptional elongation requires DNA break-induced signalling. *Nat Commun* **6**, 10191 (2015).
34. K. Kis-Toth, A. Szanto, T. H. Thai, G. C. Tsokos, Cytosolic DNA-activated human dendritic cells are potent activators of the adaptive immune response. *J Immunol* **187**, 1222-1234 (2011).
35. H. Wang *et al.*, DNA-PK-Mediated Cytoplasmic DNA Sensing Stimulates Glycolysis to Promote Lung Squamous Cell Carcinoma Malignancy and Chemoresistance. *Cancer Res* **84**, 688-702 (2024).
36. E. Erdal, S. Haider, J. Rehwinkel, A. L. Harris, P. J. McHugh, A prosurvival DNA damage-induced cytoplasmic interferon response is mediated by end resection factors and is limited by Trex1. *Genes Dev* **31**, 353-369 (2017).
37. K. R. Choi *et al.*, Fluorescence engineering in metamaterial-assisted super-resolution localization microscope. *Nanophotonics* **12**, 2491-2498 (2023).
38. M. Ovesny, P. Krizek, J. Borkovec, Z. Svindrych, G. M. Hagen, ThunderSTORM: a comprehensive ImageJ plug-in for PALM and STORM data analysis and super-resolution imaging. *Bioinformatics* **30**, 2389-2390 (2014).

Acknowledgments: We thank D. Engelberg and N. Soudah at the Hebrew University of Jerusalem in Israel for their generosity in sharing bacterial WT and mutant ERK1 and ERK2 expression vectors. We appreciate D.J. Taatjes at the University of Colorado in the USA and S. Sekine at RIKEN in Japan for critical reading and discussions and former and current members of the Bunch laboratory at Kyungpook National University (KNU) for their technical assistance. H.B thanks D.Y. Bunch, John, J.N. Park, and J. Christ for their loving encouragement and support throughout the course of this work.

Funding:

Ministry of Health, & Welfare of the Republic of Korea R5-2024-00437643 (J-HJ)

National Research Foundation of the Republic of Korea 2022R1A21003569 (HB)

Author contributions:

Conceptualization: HB

Methodology: JHC, YUL, HB

Investigation: SJ, JJ, SL, BJ, ST, HB

Visualization: SJ, JJ, HB

Funding acquisition: J-HJ, HB

Project administration: J-HJ, YUL, SKC, HB

Supervision: JHC, J-HJ, YUL, SKC, HB

Writing – original draft: HB

Writing – review & editing: YUL, SKC, HB

Competing interests: Authors declare that they have no competing interests.

Data and materials availability: All data are available in the main text or the supplementary materials.

Supplementary Materials

Materials and Methods

Figs. S1 to S5

Table S1

References (*37–38*)

Movie S1

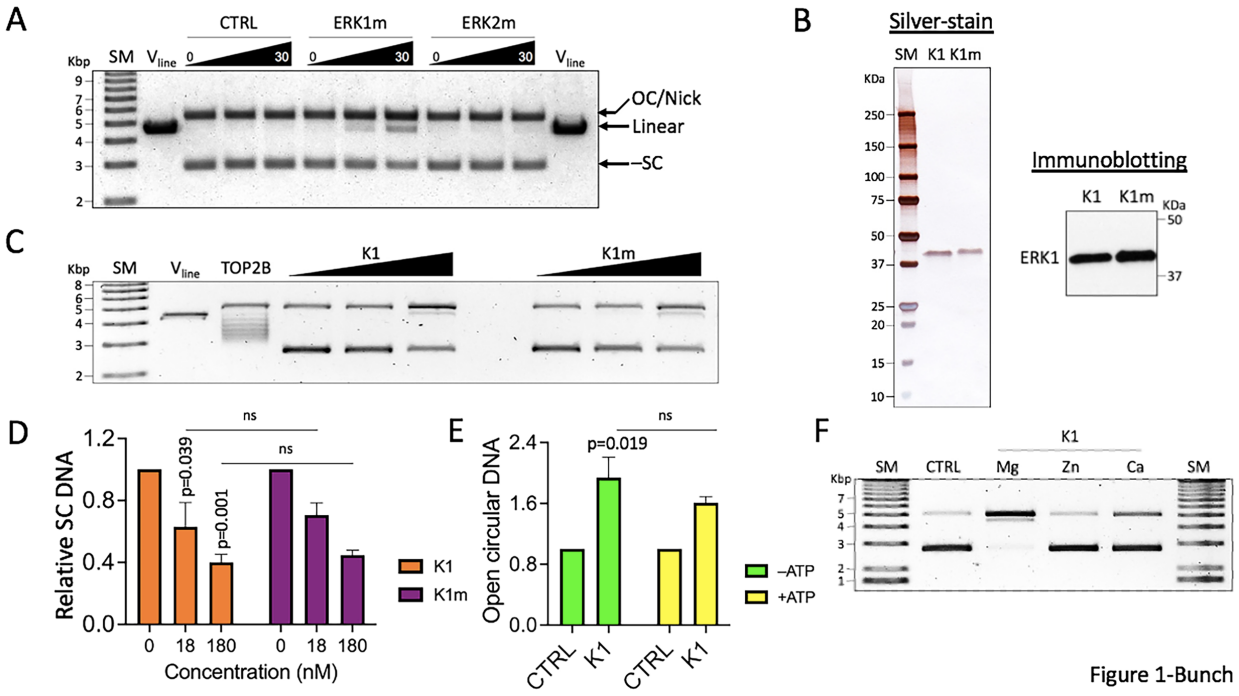

Fig. 1. ERK1 relaxes circular, supercoiled DNA. (**A**) ERK proteins (200 ng or 4.6 pmol per each reaction) with a constitutively active kinase function ($R^{84}S$ [ERK1m] and $R^{67}S$ [ERK2m], respectively) were compared for their activities to relax pBR322 in time course, 0, 10, and 30 min. Unless otherwise indicated, 250 ng (3.53 nM) of pBR322 was used per a reaction. SM, size marker; V_{line}, pBR322 linearized by HindIII; CTRL, ERK1 storage buffer only control; OC/nick, open-circular or nicked plasmid DNA; Linear, linearized plasmid DNA; –SC, negatively supercoiled plasmid DNA. (**B**) Purified ERK1 (K1) and ERK1m (K1m) proteins were visualized by silver-staining and their identity confirmed by immunoblotting. (**C**) Relaxation assay-gel showing both K1 and K1m comparably relax supercoiled pBR322 in a dose-dependent manner (0, 18, and 180 nM). pBR322 relaxed by TOP2B (2.8 fmol) was included as a comparison. (**D**) Quantification of relaxation assay results with K1 (orange bars) and K1m (purple bars) as mean values (n = 3) and standard deviation (SD). *P*-values were calculated with the unpaired, one sided Student's t-test. ns, non-significant. (**E**) Relaxation assay data with K1 and pBR322 in reactions ± ATP (0 or 1 mM final concentrations, green and yellow bars, respectively). The data were presented as mean values (n = 3) and SD. *P*-values were calculated with the unpaired, one sided Student's t-test. (**F**) Relaxation assay data showing K1 dependence on Mg^{2+} (Mg, 10 mM) for endonuclease activities. Zn^{2+} and Ca^{2+} were supplemented as 200 μM and 100 μM, respectively. Divalent ion final concentrations were determined considering their physiological concentrations. Note that linearized pBR322 DNA runs close to open circular one in (**C**) and (**F**) for the percentage of agarose gels (0.8%), compared to other gels (1.0 %).

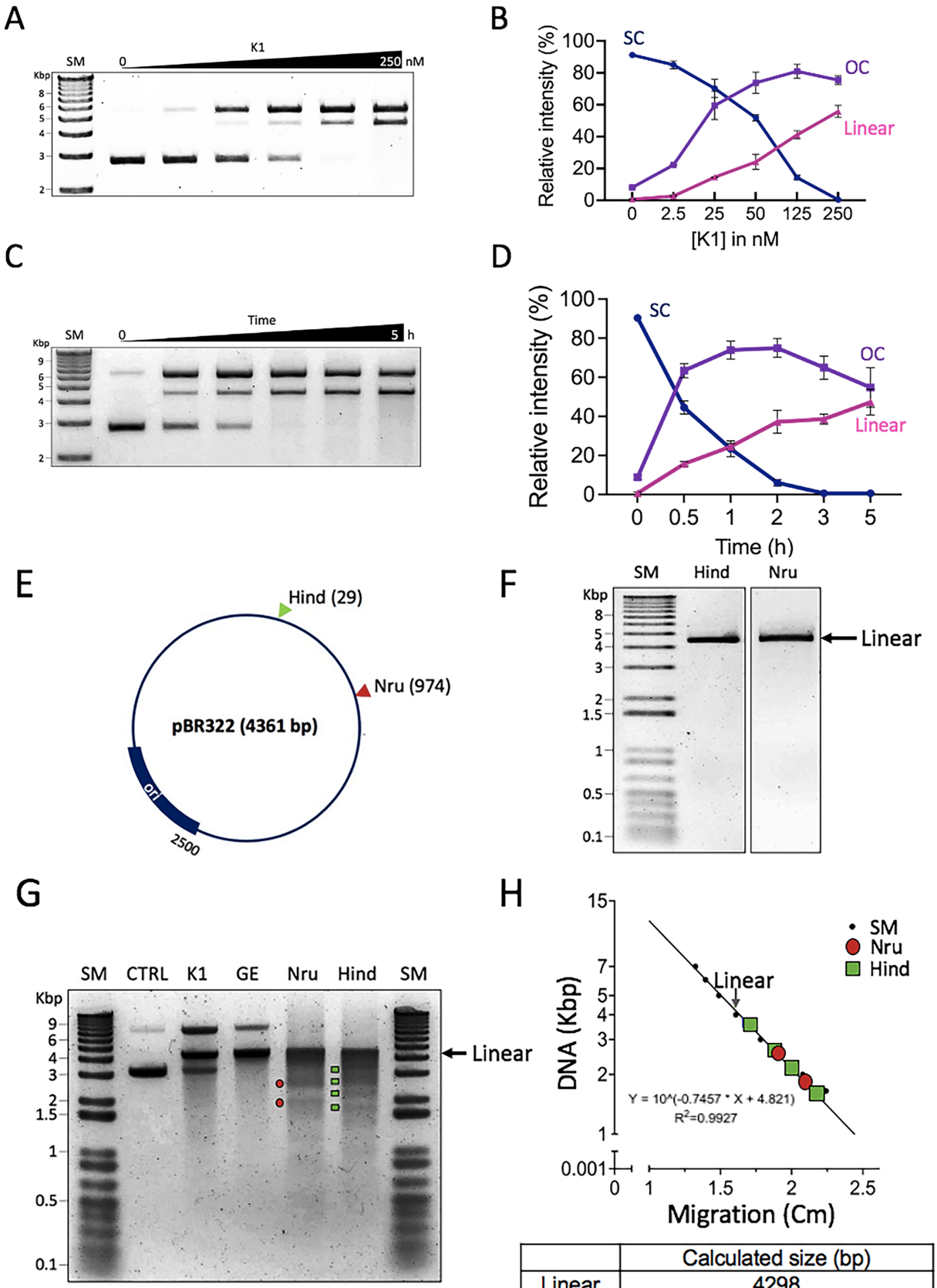

	Calculated size (bp)
Linear	4298
Nru	2536 and 1824
Hind	1629, 2181, 2699, and 3654

Figure 2-Bunch

Fig. 2. ERK1 catalyzes random single-strand DNA break. (**A**) Relaxation assay-gel showing ERK1 (K1) concentration titration (0, 2.5, 25, 50, 125, and 250 nM) for 3 h. (**B**) Quantification of the relaxation assay data of K1 concentration titration ($n \geq 3$). (**C**) Relaxation assay-gel showing pBR322 relaxation by K1 in time course analysis (0, 0.5, 1, 2, 3, 5 h). (**D**) Quantification of the relaxation assay data with K1 and pBR322 in time course analysis ($n \geq 3$). (**E**) pBR322 map showing HindIII (Hind), NruI (Nru), and *ori* sites. (**F**) Agarose gels showing a single cut of pBR322 by either Hind or Nru. (**G**) K1-mediated linearized pBR322 (K1) was gel-extracted (GE), and digested by NruI (Nru) or HindIII (Hind). CTRL, pBR322. (**H**) A simple linear regression line and equation derived from the relation between DNA migration distance and molecular weights of size marker DNA fragments (Kbp). The visible bands, after each restriction enzyme cut the K1-mediated linearized pBR322, were calculated based on the equation.

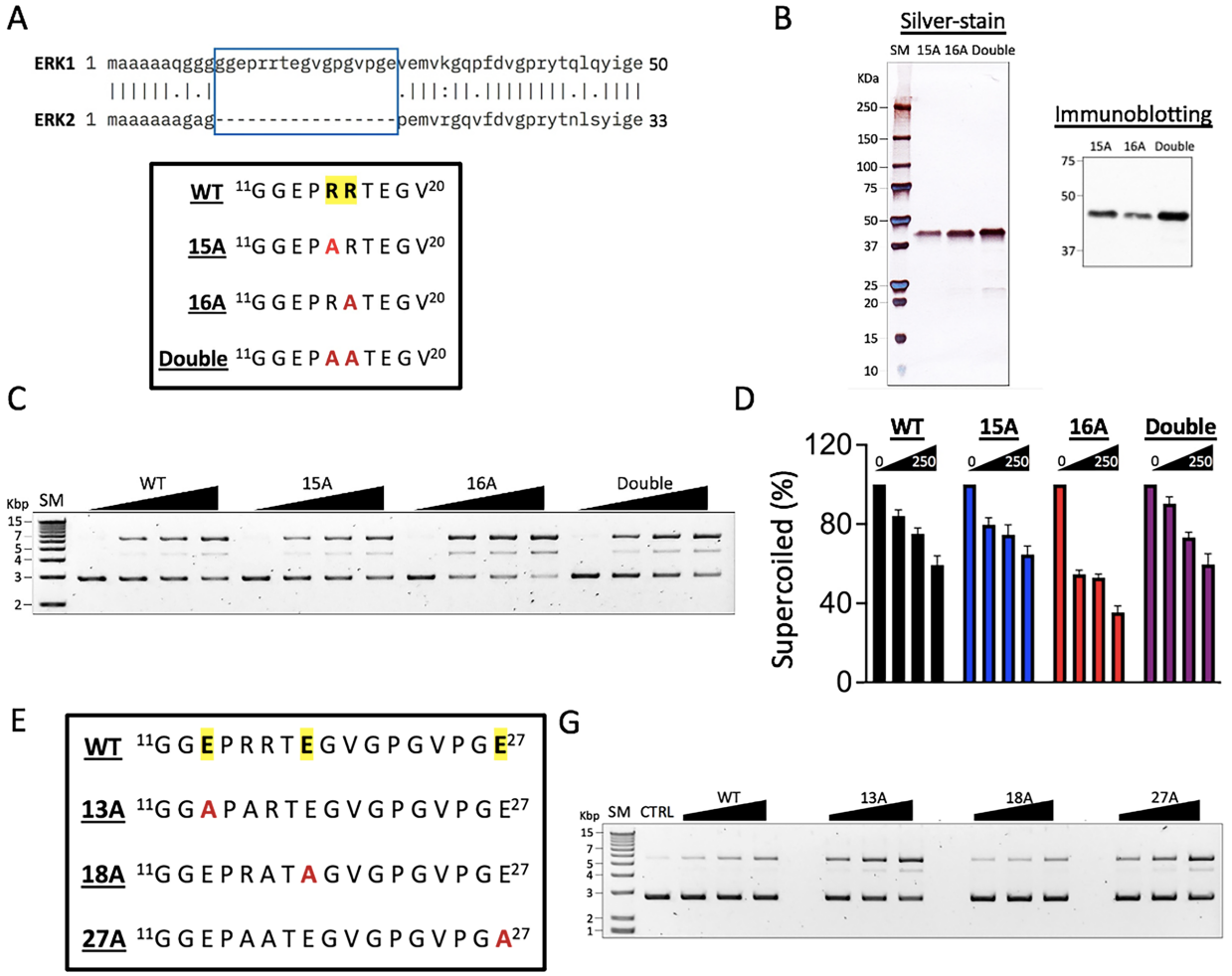
A
ERK1 1 maaaaaqggggeprrtegvgpgvpgevemvkgqpfdvgprytqlqyige 50
ERK2 1 maaaaaagag----------pemvrgqvfdvgprytnlsyige 33
WT 11G G E P R R T E G V20
15A 11G G E P A R T E G V20
16A 11G G E P R A T E G V20
Double 11G G E P A A T E G V20
B
Silver-stain
SM 15A 16A Double
KDa
Immunoblotting
15A 16A Double
C
Kbp SM
WT
15A
16A
Double
D
WT
15A
16A
Double
Supercoiled (%)
E
WT 11G G E P R R T E G V G P G V P G E27
13A 11G G A P A R T E G V G P G V P G E27
18A 11G G E P R A T A G V G P G V P G E27
27A 11G G E P A A T E G V G P G V P G A27
G
Kbp SM CTRL
WT
13A
18A
27A

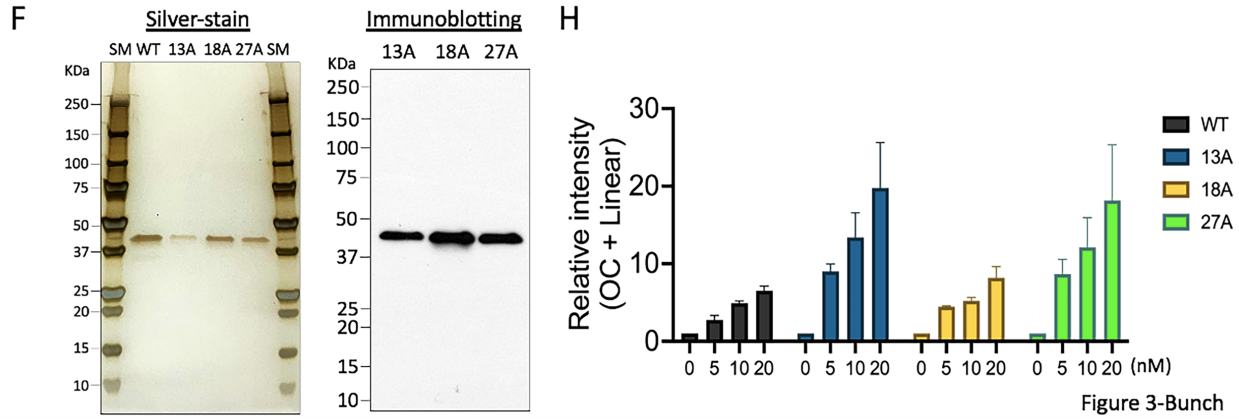
F
Silver-stain
SM WT 13A 18A 27A SM
KDa
Immunoblotting
13A 18A 27A
H
Relative intensity (OC + Linear)
WT
13A
18A
27A
(nM)
Figure 3-Bunch

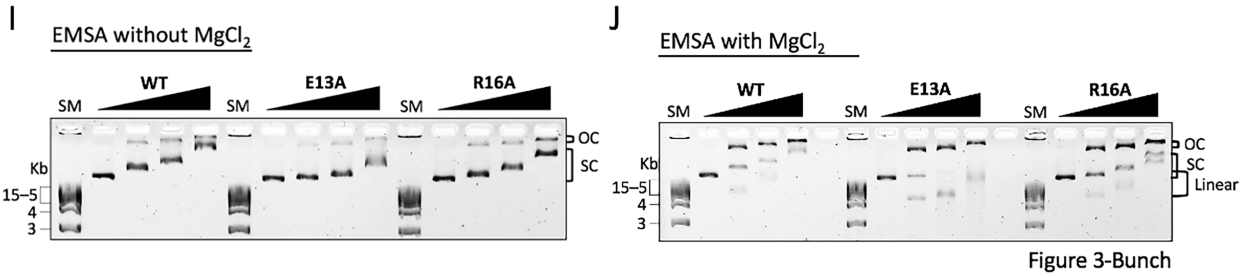
I
EMSA without MgCl2
WT
E13A
R16A
SM
Kb
OC
SC
J
EMSA with MgCl2
Linear
Figure 3-Bunch

Fig. 3. N-terminal domain of ERK1 determines nucleolytic efficiency. (**A**) Top, comparison of the N-terminal domain of ERK1 and ERK2. The region present only in ERK1 was boxed in sky-blue (11 – 27 a.a.). Bottom, R^{15} (R15) and R^{16} (R16) were marked with yellow. Three missense mutants with alanine substitutions were depicted as letter A (alanine) in red. (**B**) Purified $R^{15}A$ (15A), $R^{16}A$ (16A), and Double ($R^{15}A/R^{16}A$) mutant ERK1 proteins were visualized by silver-staining and confirmed by immunoblotting. (**C**) pBR322 relaxation by ERK1 mutants for 15 min in concentration titration (0, 60, 120, and 200 nM). (**D**) Quantification of reduced negatively supercoiled pBR322 bands by WT (black bars), 15A (blue bars), 16A (red bars), and Double mutant (purple bars) ERK1 in the concentration titration analyses (n = 3). (**E**) Three glutamates of E^{13}, E^{18}, and E^{27} (marked with yellow) were substituted to alanines (A, marked in red) (**F**) Purified $E^{13}A$ (13A), $E^{18}A$ (18A), and $E^{27}A$ (27A) ERK1 proteins were visualized by silver-staining and confirmed by immunoblotting. (**G**) Concentration titration of WT, 13A, 18A, and 27A (0, 5, 10, and 20 nM; 15 min reaction time). (**H**) Quantification of increased OC or linear pBR322 bands by WT (grey), 13A (blue), 18A (yellow), and 27A (green) ERK1 in the concentration titration analyses (n = 3). (**I**) EMSA with pBR322 (1 nM) and WT, 13A, and 16A ERK1 (0, 1, 2.5, and 5 μM) in the absence of $MgCl_2$, and (**J**) in the presence of $MgCl_2$.

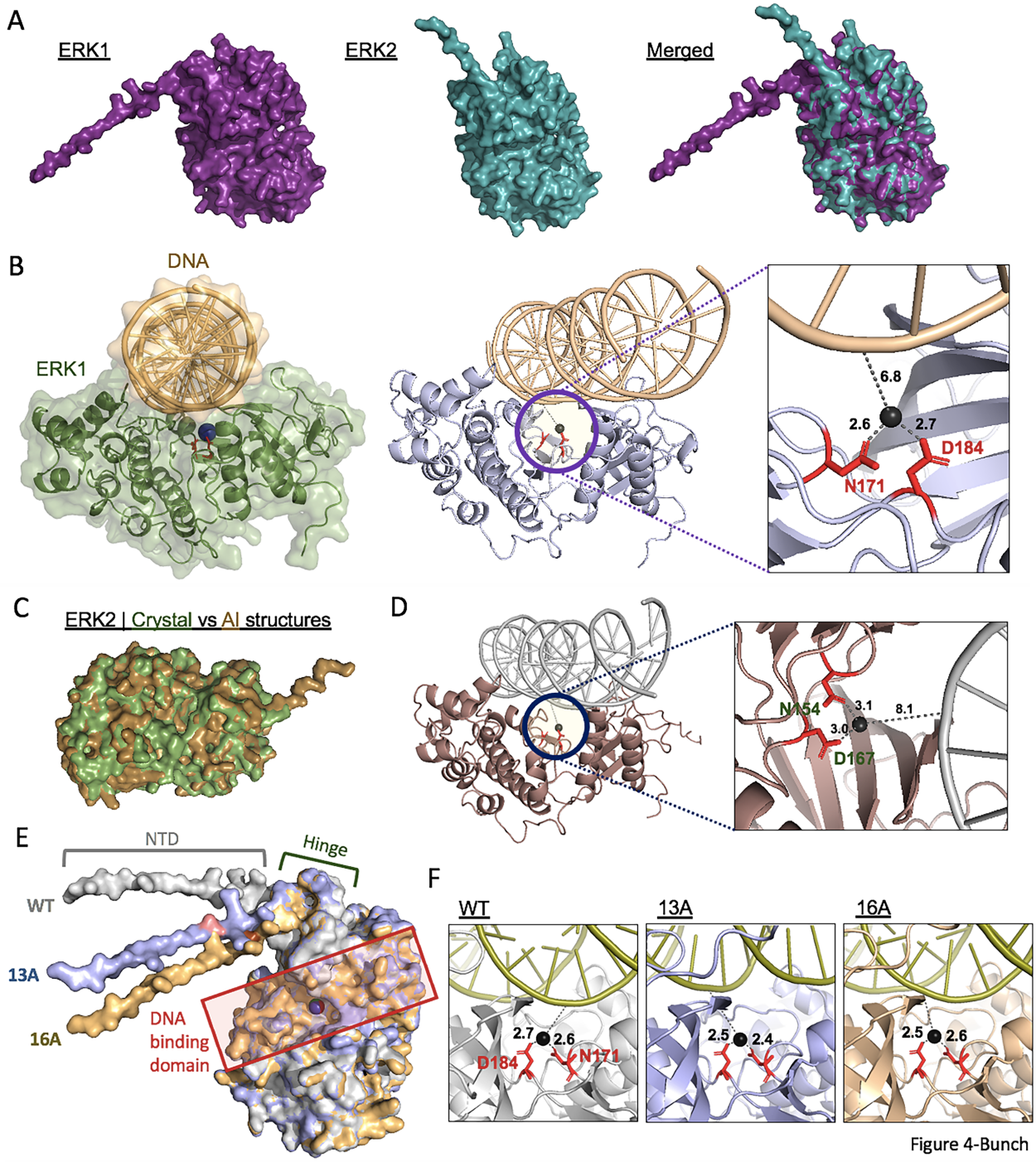

Figure 4-Bunch

Fig. 4. AI-predicted ERK1 structure model. (**A**) Left, AI-predicted ERK1 structure; middle, AI-predicted ERK2 structure; right, ERK1-ERK2 merged structures. (**B**) Left, 3D structure of ERK1 (green) and DNA (tan) complex in space-fills. Mg^{2+} in dark blue. N^{171} and D^{184} in red sticks. Middle, the complex omitting space-fills and the area with a purple circle showing the putative catalytic site of ERK1 (silver) as an endonuclease and in a zoom-in view (right). Mg^{2+}, a black sphere. Atomic distances (Å) shown in gray, dashed lines and numbers. (**C**) Merged crystal (green, PDB ID: 4H3Q) and AI-predicted (gold) ERK2 structures. (**D**) AI-predicted ERK2-DNA complex with a blue circle showing a Mg^{2+} (A black sphere) binding site (left) and a zoom-in view (right). N^{154} and D^{167} shown in red stick. (**E**) Merged structures of WT (light gray), 13A (light blue), and 16A (light orange) ERK1. The $E^{13}A$ residue in 13A and the $R^{16}A$ residue in 16A were marked in pink and orange, respectively. NTD, N-terminal domain; Mg^{2+} in black (WT), dark blue (13A), and red (16A); DNA binding cleft/domain boxed in red. (**F**) Comparison of distances between Mg^{2+} and two coordinating amino acids, N^{171} and D^{184} in WT and 13A and 16A mutant ERK1 proteins. The same DNA (28-mer, 2292–2319 of pBR322) was used in **Fig. 4**, **B, D,** and **F**.

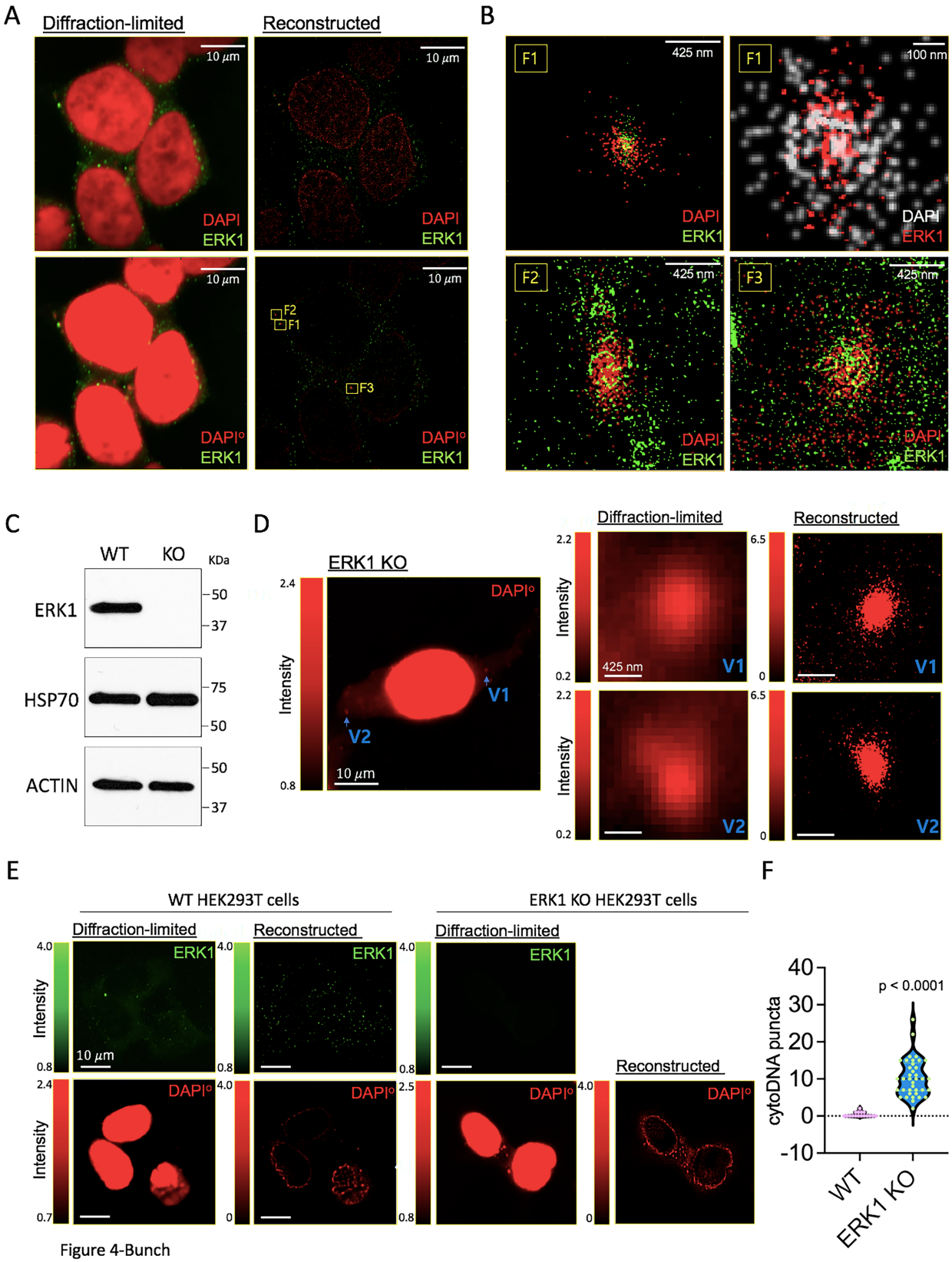

Figure 4-Bunch

Fig. 5. ERK1 interacts with and destabilizes cytoplasmic DNA. (**A**) Diffraction-limited and reconstructed super-resolution multicolor images of ERK1 KO cells. Top, diffraction-limited (left) and super-resolution (right) fluorescence images. DAPI (red) and ERK1 (Alexa 647, green). Bottom, overexposed DAPI (DAPI^{o}) merged with ERK1 (left) and the super-resolution image excluding oversaturated DAPI signals (right). F1–3, focal sites of DAPI and ERK1 overlapping signals. Intensity scales should be multiplied by 10^4 in arbitrary units (AU) throughout **Fig. 5**. (**B**) Zoom-in views of F1–3 showing cytoDNA-ERK1 interaction. (**C**) Validation of WT and ERK1 KO HEK293T cells by immunoblotting. β-ACTIN and HSP70 as reference and loading controls. (**D**) Cytoplasmic DAPI puncta (red) in an ERK1 KO HEK293T cell (left). V1–2 sites were magnified in diffraction-limited and super-resolution microscopy images (right). (**E**) Diffraction-limited and super-resolution microscopy images of WT and ERK1 KO cells showing colocalization of ERK1 (Alexa 647, green) and DNA (DAPI^{o}, red). (**F**) Quantification of cytoplasmic puncta revealing a significant increase in ERK1 KO cells (blue violin, n = 38) compared to WT cells (pink violin, n = 17). The data were presented as mean values and SD. *P*-values were calculated with the unpaired, two-sided Student's t-test.